Working Together: Spatial Synchrony in the Force and Actin Dynamics of Podosome First Neighbors

Amsha Proag,[†,‡,⊗] Anaïs Bouissou,[†,‡,⊗] Thomas Mangeat,[‡,§] Raphaël Voituriez,[⊥] Patrick Delobelle,[∥] Christophe Thibault,[#,▽] Christophe Vieu,[#,▽] Isabelle Maridonneau-Parini,[*,†,‡] and Renaud Poincloux[*,†,‡]

[†]IPBS (Institut de Pharmacologie et de Biologie Structurale), UMR CNRS 5089, 205 route de Narbonne, F-31077 Toulouse, France, [‡]UPS, Université de Toulouse, F-31400 Toulouse, France, [§]CNRS, LBCMCP, 118 route de Narbonne, F-31400 Toulouse, France, [⊥]UPMC, Laboratoire Jean Perrin, FRE 3231 CNRS-UPMC, 4 place Jussieu, F-75005 Paris, France, [∥]FEMTO-ST, UMR CNRS 6174, Université de Franche Comté, 24 rue de l'Epitaphe, F-25000 Besançon, France, [#]CNRS, LAAS, 7 avenue du colonel Roche, F-31400 Toulouse, France, and [▽]INSA, Université de Toulouse, F-31400 Toulouse, France. [⊗]A.P. and A.B. contributed equally to this work.

ABSTRACT Podosomes are mechanosensitive adhesion cell structures that are capable of applying protrusive forces onto the extracellular environment. We have recently developed a method dedicated to the evaluation of the nanoscale forces that podosomes generate to protrude into the extracellular matrix. It consists in measuring by atomic force microscopy (AFM) the nanometer deformations produced by macrophages on a compliant Formvar membrane and has been called protrusion force microscopy (PFM). Here we perform time-lapse PFM experiments and investigate spatial correlations of force dynamics between podosome pairs. We use an automated procedure based on finite element simulations that extends the analysis of PFM experimental data to take into account podosome architecture and organization. We show that protrusion force varies in a synchronous manner for podosome first neighbors, a result that correlates with phase synchrony of core F-actin temporal oscillations. This dynamic spatial coordination between podosomes suggests a short-range interaction that regulates their mechanical activity.

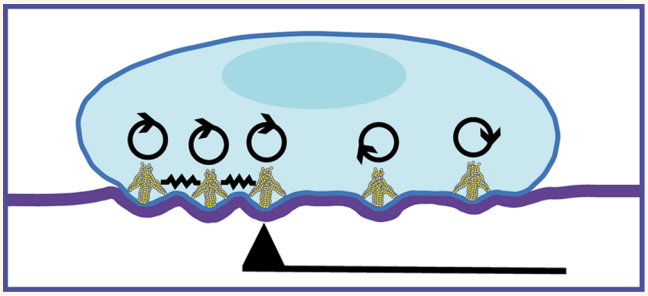

KEYWORDS: cell mechanics · podosome · atomic force microscopy · synchrony · neighbors · macrophage · protrusion force microscopy

Forces exerted by a single cell on its environment were first brought to attention by Harris and co-workers,[1] when a fibroblast was shown to produce wrinkles on the silicon elastic film it was plated on. Since then, many techniques collectively known as traction force microscopy have been developed in order to measure the nanoscale forces exerted by adherent cells on their environment *via* focal adhesions.[2−4] Indeed, these adhesion structures enable transmission to the substrate of traction forces produced by the cellular acto-myosin machinery, which results in measurable substrate deformation.[5] The common principle of traction force evaluation resides in the measurement of the displacement of substrate-bound probes and its conversion into stress or force values.[6]

Cells can also exert protrusive forces toward their environment, which is typified by podosomes. Found in macrophages, dendritic cells and osteoclasts, podosomes form at the ventral plasma membrane and are oriented perpendicularly to the substrate. They consist of a 500 nm-high columnar core of F-actin surrounded at its base by a ring of adhesion proteins and proteins linking the actin cytoskeleton to the substrate *via* integrins.[7,8] They are also very dynamic cell structures, with a typical lifetime of 10 min, and display spatial and compositional instabilities.[9−11] Like focal adhesions, podosomes possess mechanosensing properties,[12,13] which requires them to exert forces on the environment to probe its mechanical properties. In this regard, it was proposed that podosomes could protrude in the extracellular environment,[14−17] a property recently demonstrated by our work.[13]

We have previously designed and developed a setup to evaluate the nanoscale

* Address correspondence to renaud.poincloux@ipbs.fr, isabelle.maridonneau-parini@ipbs.fr.

Received for review November 26, 2014 and accepted March 19, 2015.

Published online March 20, 2015
10.1021/nn506745r

forces generated by podosomes, called protrusion force microscopy (PFM).[13] This consists in plating macrophages on an elastic membrane on which podosomes form, measuring by atomic force microscopy (AFM) the subsequent nanometer deformations of this membrane on its reverse side and finally evaluating the corresponding force. Using this method, we have demonstrated that both actin polymerization and acto-myosin contractility are required for the podosome to deform the substrate. This has helped us develop a physical model of how a single podosome generates a dynamic protrusion force. The podosome core is composed of a bundle of actin microfilaments polymerizing at the cell membrane, thus exerting a pushing force against the substrate. Simultaneously, lateral contractile acto-myosin cables connect the core to the adhesion ring, through which they pull on the substrate. Furthermore, we have shown that substrate deformation by single podosomes exhibits an oscillatory behavior, as predicted by dynamic analysis of this two-component model when protrusion and traction forces balance each other.

Podosomes are scattered and interconnected through a radial F-actin cable network.[13,18,19] It has been suggested that the regulation of podosome spatial organization is the basis for higher-ordered dynamic cellular structures such as podosome rosettes, belts and sealing zones.[20,21] Therefore, it is necessary to inquire whether spatial coordination of podosomes exists.

Our present objective is thus to investigate to what extent protrusion force oscillations at podosome sites correlate between neighbors. We first developed an automated procedure for protrusion force evaluation that takes into account podosome architecture and organization. We performed time-lapse PFM and total internal reflection fluorescence (TIRF) microscopy on live human macrophages differentiated from primary monocytes to follow the dynamics of podosome pairs. We report spatial phase synchrony of the temporal variations of podosome neighbors both regarding protrusion force and core F-actin oscillations.

RESULTS AND DISCUSSION

Finite Element Simulations of Substrate Deformation by Podosomes. Macrophages plated on a suspended Formvar membrane form podosomes that push against this substrate and produce nanoscale bulges. AFM analysis of the opposite surface of the Formvar membrane provides a topographical image of the deformations (Figure 1a–c).

In order to evaluate force from deformation measurements, we carried out numerical simulations of Formvar deformation by podosomes as a means to take into account podosome architecture and organization. The mechanical action of podosomes was modeled by a module that integrated geometrical data regarding podosome architecture[22,23] into the two-component representation of core polymerizing actin filaments and contractile acto-myosin cables connected to the adhesion ring.[13]

In this perspective, the substrate is subjected to two equal and opposite forces: a traction force under the adhesion ring, oriented toward the cell, and a central pressure under the core, oriented in the opposite direction. Traction on the substrate was modeled by stress-based boundary conditions: the adhesion ring domain was subjected to a uniform total traction force (Figure 1d) balancing the central protrusion force (see details in the Methods section). Finite element simulations of arrays of such modules show relief variation of the Formvar membrane around and between individual podosomes (Figure 1e,f), in accordance with the experimental PFM observations (Figure 1c).

As traction is applied at the adhesion ring, we chose to measure the deformation of the Formvar membrane as the difference h between the peak height and the height at the ring (Figure 1f). We checked that this quantity h, called the deformation height, was proportional to applied force F_p (Figure 2a) for a given set of geometrical parameters, which showed its relevance as a force indicator. Indeed, having properly defined the boundary conditions, we could reasonably expect to calculate the force unequivocally from deformation height, provided the deformation-to-force ratio (h/F_p) is known.

Influence of the Substrate Thickness and Podosome Architecture on the Force–Deformation Relationship. To characterize the force–deformation relationship of the protrusion-traction modules, we performed series of simulations while varying, one by one, the geometrical parameters: the thickness h_f of the Formvar membrane, the actin core radius r_p, the adhesion ring radius r_t and width w (Figure 1d) and the interpodosome distance d.

For a given force, the deformation height values vary up to hundred-fold as membrane thickness takes typical experimental values, *i.e.*, from 20 to 90 nm (Figure 2a). More precisely, the behavior of h/F_p with respect to h_f can be fitted with an inverse cubic function (Figure 2b, $R^2 \approx 0.9998$). Similarly, h/F_p may vary up to 10-fold as traction ring radius lies between 200 and 500 nm (Figure 2c). Its behavior as a function of r_t can be well described using a square function (Figure 2d, $R^2 \approx 0.98$). With all other parameters fixed, the deformation height displays a 2-fold variation for core radius r_p values under 300 nm (Figure 2e). Finally, when the ring width w was varied from 10 to 250 nm, the deformation-to-force ratio h/F_p remained around 0.7 $m \cdot N^{-1}$ with a less than 5% relative variation, which was considered to be negligible.

These data show that the accuracy of the Formvar membrane thickness is essential to reduce the uncertainties

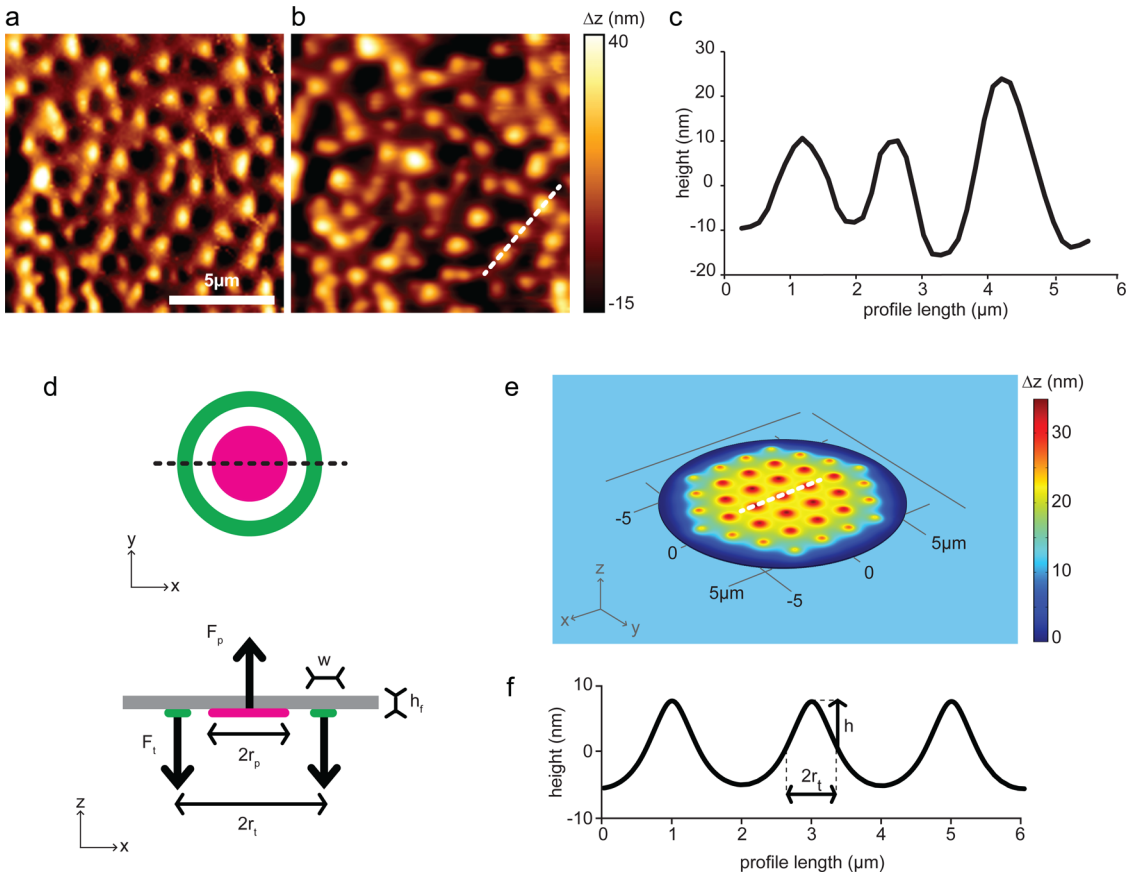

Figure 1. A two-component protrusion-traction module approximates the deformation profile. (a–c) Podosome-induced deformations onto a Formvar membrane, imaged by AFM in contact mode (a: vertical deflection, b: height, c: profile of the dotted line in (b)). (d) Protrusion-traction model used for the numerical simulation of substrate deformation by a podosome. (e,f) Simulation results of the deformation of a Formvar plate by a hexagonal lattice of 37 protrusion-traction modules. The profile (f) is drawn from the deformation map (e), and the deformation height h is measured on the profile as the difference between peak height and height at the ring. Parameters for this simulation: h_f = 60 nm, r_t = 450 nm, r_p = 100 nm, w = 100 nm, F_p = 50 nN and d = 2 μm as center-to-center interpodosome distance.

in force evaluation, followed in decreasing order by traction ring radius and core radius.

Influence of Interpodosome Distance on the Force–Deformation Relationship. To evaluate to what extent the presence of neighbors alters the deformation height value, simulations were performed in which the interpodosome distance d was varied between 0.8 and 2.5 μm. The deformation-to-force ratio h/F_p was measured as a function of d in an isotropic configuration, *i.e.*, where all podosome modules are equidistant (h_{iso}) (Figure 2f,g). This shows that for a given force, the deformation height gains 50% when d varies from 800 nm to 1.5 μm, whereafter it increases more and more slowly, with a mere 6% increase from 1.5 to 2 μm (Figure 2g).

A different configuration was used to assess the influence of podosome spatial arrangement. In a podosome array where every podosome is located 2 μm apart from its neighbors, a single neighbor ("*b*" on Figure 2f) of the central podosome "*a*" is moved while the other neighbors of "*a*" remain fixed. In order to take into account the anisotropic deformation, the deformation-to-force ratio of protrusion "*a*" was measured toward all six neighbors of "*a*", at each 60° angle. When measured on the (*ab*) axis in the direction of "*b*", h/F_p decreased when "*b*" got closer to "*a*" (Figure 2h, h_{cis}). However, the average ratio, totalling the six values of h/F_p measured on protrusion "*a*" in all six directions (including toward "*b*"), was found to be independent of the distance d_{ab} (Figure 2h, h_{avg}).

Hence, the nearest-neighbor counts for little in the deformation height averaged on all neighbors, which is one of the main findings of the simulation results. As a practical consequence, we will only need to take into account the average distance of all the neighbors when evaluating force from deformation measurements, instead of the actual distance of every neighbor.

In the light of the simulation results, we can write the force–deformation relationship as

$$\frac{h}{F_p} = \frac{1}{C}\frac{r_t^2}{h_f^3}$$

From the perspective of thin plate theory, the Formvar membrane may be considered as a thin plate of linear elastomer on which forces applied on a disk produce a

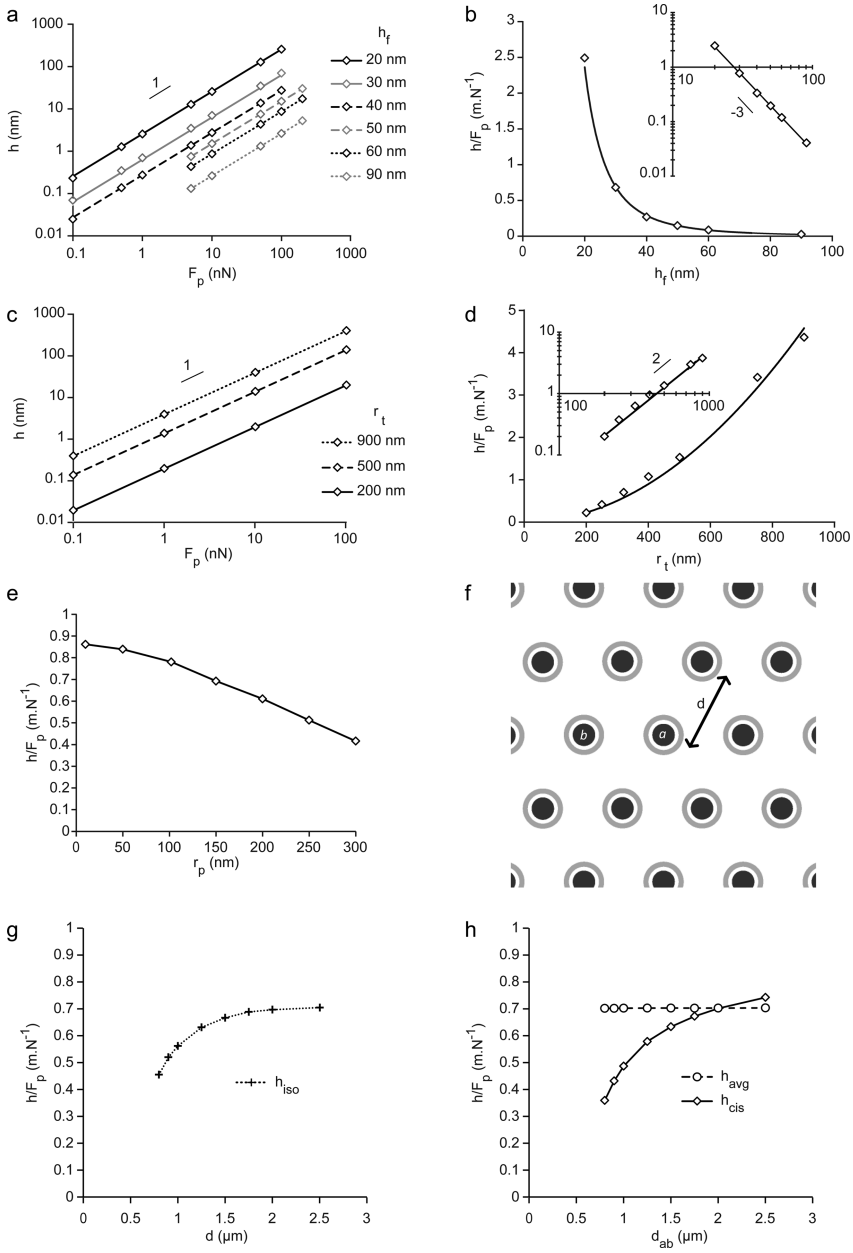

Figure 2. Influence of protrusion force, podosome architecture and substrate thickness on the deformation height. (a) Deformation height h as a function of applied force F_p, for Formvar membranes of different thickness h_f. (b) Deformation-to-force ratio as a function of membrane thickness h_f, with axes in linear and logarithmic (inset) scales. (c) Deformation height h as a function of applied force F_p, for traction rings of different radius r_t. (d) Deformation-to-force ratio as a function of traction ring radius r_t, with axes in linear and logarithmic (inset) scales. (e) Deformation-to-force ratio as a function of core radius r_p. (f) Array of podosome modules separated from each other by a center-to-center distance d. In the isotropic configuration (g), the distance d_{ab} between podosomes a and b is equal to d; in the anisotropic configuration (h), d is fixed at 2 μm while b moves toward a (d_{ab} varies). (g) Deformation-to-force ratio as a function of interpodosome distance d in the isotropic configuration. (h) Deformation-to-force ratio as a function of d_{ab} in the anisotropic configuration where all podosomes remain at $d = 2$ μm from each other except for podosome b, which moves toward a. h_{cis} is measured on podosome a in the direction of b and h_{avg} is the average deformation height-to-force ratio measured in all six neighbors' directions. Throughout these series of simulations, parameters that did not vary had the following values: $h_f = 30$ nm, $r_t = 350$ nm, $r_p = 150$ nm, $w = 25$ nm, $d = 2$ μm.

small deformation with no displacement constraint. Its bending modulus is then given by $K \sim Eh_f^3$.[24] The energy cost of the deformation induced by a podosome is controlled by bending and can be written $e \sim KS/R_C^2$ where $S \sim r_t^2$ is the area of the deformation and $R_C \sim r_t^2/h$ is the local radius of curvature. This yields $e \sim Eh_f^3h^2/r_t^2$ and eventually

$$F_p = \frac{de}{dh} \sim \frac{Eh_f^3}{r_t^2} h$$

the scaling of which is consistent with our numerical simulations.

After rewriting of the force−deformation relationship as

$$F = C_0 \frac{E}{1-\nu^2} \frac{{h_f}^3}{{r_t}^2} h$$

where $E/(1-\nu^2)$ is the biaxial Young's modulus, the boundary conditions, and in particular the influence of r_p and d corresponding to Figure 2e,g, are taken into account in $C_0 = f(\nu, r_p/r_t, d/r_t)$, which can be determined numerically thanks to the present model.

Measurement of Podosome Geometrical Parameters. To use this formula to obtain force values from experimental deformation height measurements, we need to measure the actual values of the relevant parameters as follows.

First, the thickness h_f of the Formvar membrane is measured for each series of experiments by AFM, as detailed in the Methods section.

Second, the ring radius r_t and core radius r_p are measured with immunofluorescence staining of unroofed macrophages (Figure 3a−d). After deconvolution, podosomes were identified as local maxima of fluorescence intensity maxima and then quantified using an intrinsic definition of the borders of cores and rings, based on the amplitude of spatial gray-level variation instead of an intensity threshold (see Figure 3e−j and the Methods section). Macrophages plated on Formvar exhibited an average vinculin ring radius of r_r = 350 nm ± 15% and width of $r_e - r_i$ = 200 nm ± 12%, and an actin core radius of r_c = 140 nm ± 16%. Importantly, podosomes possessed the same characteristics whether the cells were plated on Formvar or on glass (Figure 3k). This indicates that measurement of podosome characteristics may be performed on glass prior to force evaluation.

To verify the apparent core radius measured by immunofluorescence, scanning electron microscopy (SEM) was performed on the ventral membrane of inverted macrophages. SEM images of inverted cells showed smooth protruding islands (Figure 3l−o) with the typical arrangement and dimensions of podosomes. The radius of these islands averaged out to 220 nm ± 24% (Figure 3p), which is close to, and confirms, the value of r_c obtained above.

Third, to estimate the interpodosome distance, direct neighbors were defined using the Delaunay triangulation on podosome arrays extracted from fluorescence images (Figure 3q,r).[25] The average distance to neighbors was found to be 1.77 μm ± 34% (Figure 3s).

On the whole, these values are compatible with previous measurements of ring dimensions[22,23] and were therefore used in the force evaluation procedure explained below.

Force Evaluation from Topography Measurements. The following scheme was devised to evaluate protrusion force values from the analysis of an AFM topographical image of podosome-induced deformations onto a Formvar membrane. Given this PFM experimental data, the force applied by each podosome is deduced from the formula $F = C_0 \cdot E/(1-\nu^2) \cdot h_f^3/r_t^2 \cdot h$, where $E/(1-\nu^2)$ = 2.3 GPa,[13] h_f is measured on the Formvar sample before experiments, the value of r_t is chosen as 350 nm as measured in the previous section and h is measured on the AFM image as depicted in Figure 1f. C_0 is determined from simulations using the protrusion-traction model with the remaining parameters narrowed down to r_p = 140 nm and d = 1.75 μm in accordance with the geometry: in this configuration, $C_0 \approx 2.7$. As stressed above, the deformation-to-force ratio varies only slightly around these values of r_p and d (Figure 2e,g) and the value of w is of no account. Therefore, little uncertainty in the value of C_0 is expected from the variability of actual podosome geometry.

Nonetheless, in order to estimate the error in force evaluation, we sought to validate this procedure by simulating actual experimental measurements. Given the experimental PFM topography of podosome-induced protrusions on a Formvar membrane of known thickness (Figure 4a,b), we measured the deformation height h of each protrusion and computed the corresponding forces, which range from 2.9 to 12.2 nN (Figure 4c). Then, the same podosomes were simulated as protrusion-traction modules with uniform geometrical parameters (r_p = 140 nm, r_t = 350 nm, w = 25 nm), but located at their actual positions relative to one another, with each one exerting its respective force. The resulting deformation map (Figure 4d) was then compared to the experimental original one. As Figure 4e shows, deformation measurements on the output map differ by less than 10% from the original experimental deformation measurements. Therefore, we may conclude that despite not knowing the actual geometry of the podosomes whose protrusion is revealed by PFM, the evaluation of the corresponding protrusion force by the present method gives a reasonable value. The approach is all the more robust that this validation by experimental measurements included force heterogeneity and irregular spatial arrangement of podosomes. However, since the measurement of deformation height relies critically on the knowledge of the ring radius value, this quantity will have to be measured each time the experimental conditions make it susceptible to change notably.

We measured protrusion forces for 59 macrophages plated on 30 nm-thick Formvar, leading to a mean force value of 10.4 nN (Figure 4f). In our previous work, 3 times higher forces were calculated on the same membrane thickness. We had proceeded by fitting individual profiles of protrusion height by an analytical curve derived as the result of a punctual force acting on a circular Formvar membrane clamped at a position corresponding to the minima of the

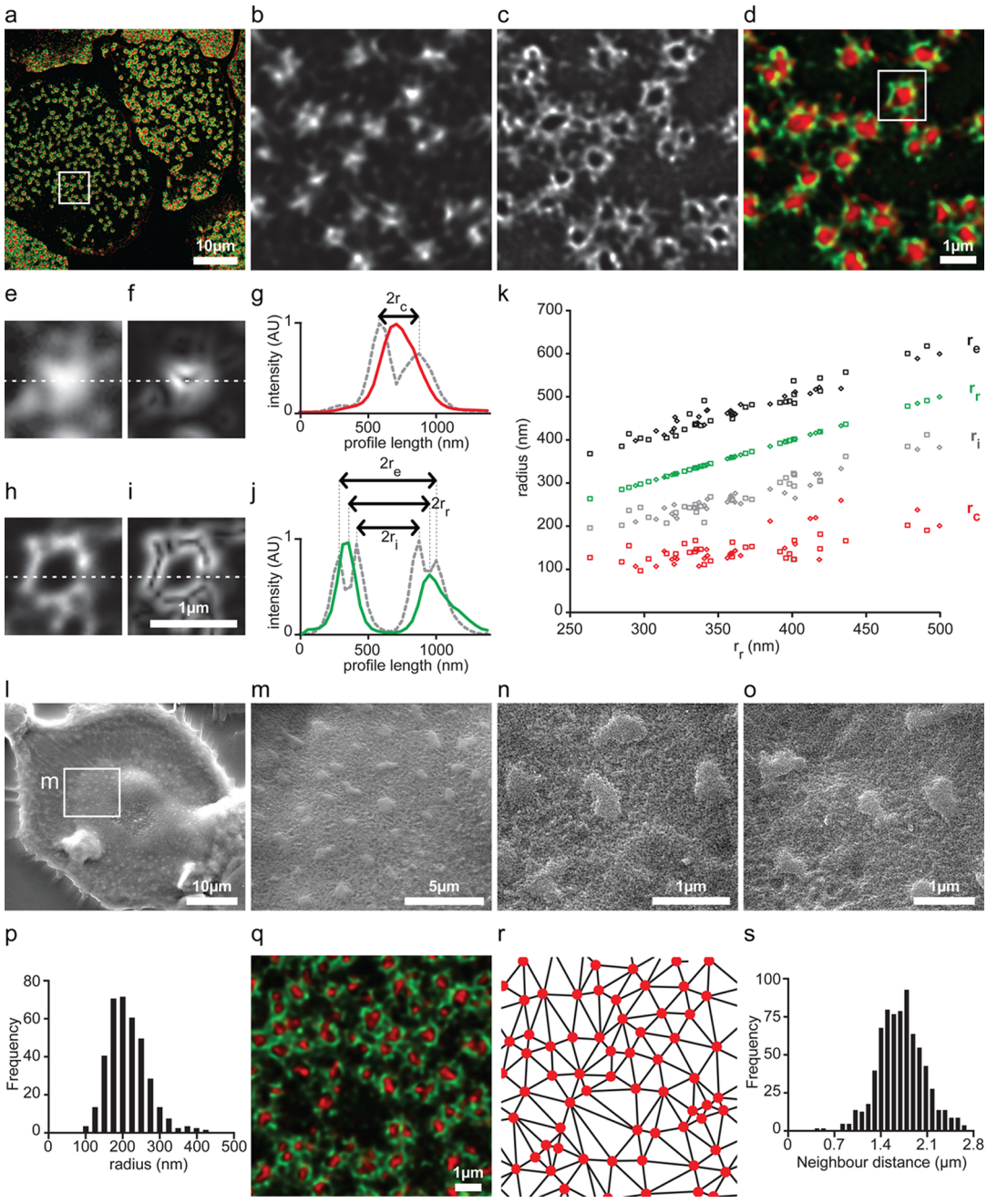

Figure 3. Measurement of the geometrical characteristics of podosomes. (a−d) Deconvolved fluorescence microscopy image of podosomes of a fixed, unroofed macrophage immunostained for F-actin (red) and vinculin (green). (b−d) Enlarged view of the region framed in (a), showing separately F-actin (b) and vinculin (c). (e,f) Enlarged view of the podosome marked in (d) showing the F-actin core (e) and its edge image, *i.e.*, its map of highest intensity variation (f). (g) Intensity profile of the cross sections in (e) (solid red) and (f) (dotted gray). The core radius r_c is defined as the distance from the core center (the actin intensity peak) to the edge intensity profile peaks. (h,i) Enlarged view of the podosome marked in (d) showing the vinculin ring (h) and its edge image (i). (j) Intensity profile of the cross sections in (h) (solid green) and (i) (dotted gray). The ring radius r_r is defined as the distance from the core center to the vinculin intensity profile peaks. The inner and outer ring radii r_i and r_e are defined as the distances from the core center to, respectively, the internal and the external peaks of the edge intensity profile. Of note, the radii were calculated from the peaks on eight cross sections (each 45°), the median value of which yielded the final radius. (k) Radii r_c (red), r_i (gray), r_r (green) and r_e (black) plotted against r_r itself. Each mark is the median of all podosomes in one cell plated on Formvar (squares) or glass (diamonds) (20 cells on each substrate, over 200 podosomes per cell). (l−o) Scanning electron microscopy (SEM) image of the ventral side of an inverted macrophage. (m−o) Enlarged views. (p) Histogram of podosome radius values measured from inverted SEM experiments (140 podosomes). (q) Deconvolved fluorescence microscopy image of podosomes of a fixed, unroofed macrophage immunostained for F-actin (red) and vinculin (green). (r) Delaunay triangulation from the cores in (q). (s) Histogram of the average distances to neighbors measured as Delaunay edges (740 podosomes).

deflection between adjacent podosomes.[13] In the present paper we have deliberately chosen to impose force-based boundary conditions, in accordance with the current biological representation of the podosome

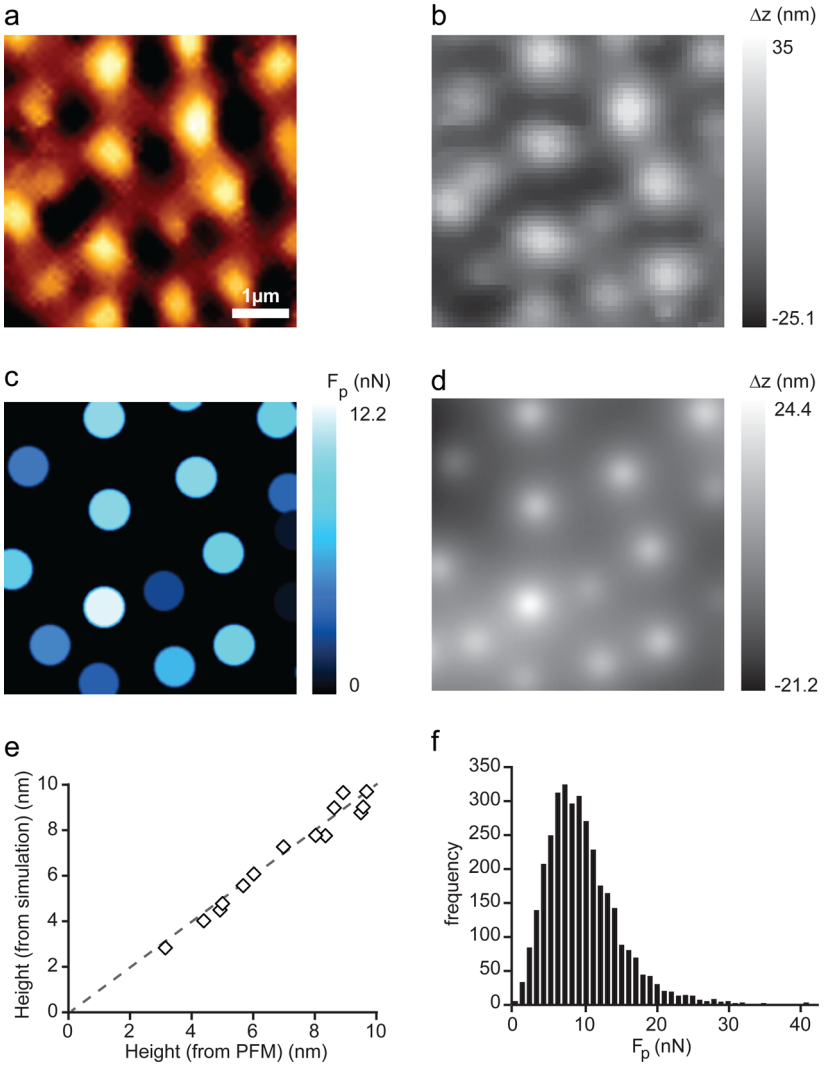

Figure 4. Force evaluation from topography measurements. (a–c) Force estimation from topography measurements. Podosome-induced deformations of a live macrophage onto a 28 nm-thick Formvar membrane, imaged by AFM in contact mode (a: vertical deflection, b: height) and corresponding force values (c) deduced from the present evaluation method. (d) Output deformation map of a simulation of podosomes in the same spatial configuration as (b), with uniform geometrical parameters (r_p = 150 nm, r_t = 350 nm, w = 25 nm) and applying the forces calculated in (c). To analyze this simulation in the same conditions as an AFM image, a parabolic fit was performed on the resulting grayscale deformation image before measuring the deformation height. (e) Comparison of the output deformation height (d) to the measured deformation height (b), over the identity region (dotted line). (f) Force distribution of podosomes in macrophages (10.4 ± 3.8 nN on 30 nm-thick Formvar, 59 cells, over 3000 podosomes).

and experimental measurements of its geometry. We have verified for individual podosomes that the analytical model[13] and the present numerical method give the same estimation of protrusion forces when the same mechanical boundary conditions are used.

Both Force and Actin Vary in Synchrony between Close Neighbors. The procedure described above was implemented in an ImageJ macro (see Methods and Supporting Information) so as to automate the successive steps, starting from PFM data processing to force evaluation, and resulting in high throughput analysis of podosome-induced protrusions. Although time-resolved force measurement had already been carried out on single podosomes,[13] with the AFM tip applying a constant force on a podosome-induced bulge, it did not allow the measurement of multiple podosomes over time, which is made possible by the present approach. Consequently, we were now able to carry out time-lapse protrusion force measurements of podosomes, by repeatedly imaging a small, 3–5 μm-wide region comprising 4–10 podosome-induced bulges (Figure 5a). In this way, force dynamics could be measured and appeared to correlate between podosome neighbors (Figure 5b).

To quantify to what extent podosome protrusion force varied concomitantly between neighbors, we defined an estimator of spatial synchrony for a pair of force curves. Instant correlation between two neighbors was assessed by a Pearson cross-correlation coefficient calculated over a sliding time window and

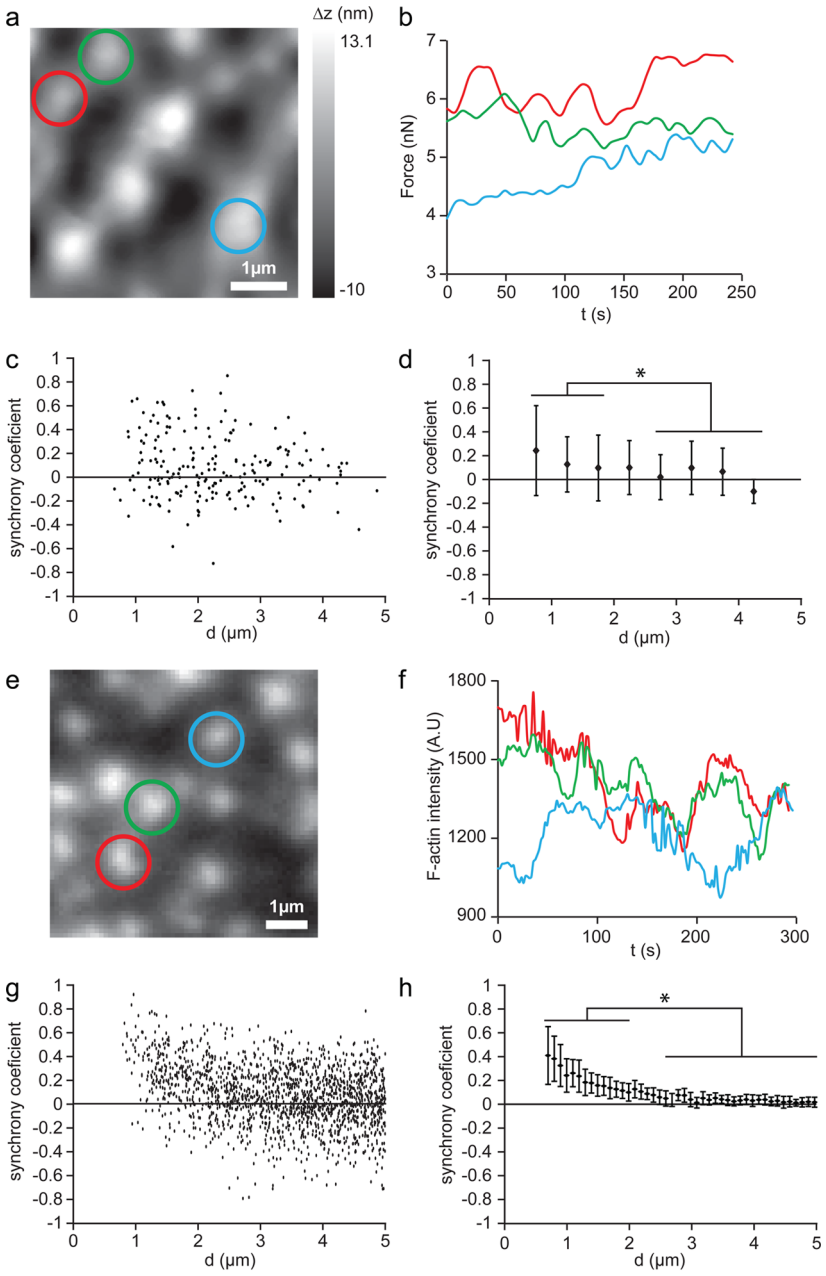

Figure 5. Force and actin synchrony between close neighbors. (a,b) Time-lapse protrusion force microscopy (PFM) experiments. Height measurements of podosome-induced deformations by a live macrophage onto a 28 nm-thick Formvar membrane at a given time (a) and force variation over time (b) of three protrusions. The synchrony coefficient is 0.42 for red *versus* green and only 0.01 for red/blue and −0.12 for green/blue. (c) Synchrony coefficient of force fluctuations of podosome pairs as a function of distance between pairs (200 podosomes pairs). (d) Average synchrony coefficient (±s.d.) of force fluctuations of podosome pairs as a function of distance (18 cell regions, 350 podosomes pairs). *t* test was used to compare pairs under 2 μm and pairs above 2.5 μm. *$p < 0.05$. (e,f) Time-lapse TIRF imaging of podosome F-actin cores within a live mCherry-Lifeact-expressing macrophage (d) and intensity variation of three podosomes over time (e). The synchrony coefficient of red *versus* green equals 0.41, whereas red/blue stand at 0.17 and green/blue at −0.04. (g) Synchrony coefficient of actin intensity fluctuations of podosome pairs as a function of distance between pairs (1783 podosomes pairs). (h) Average synchrony coefficient (±s.d.) of actin intensity fluctuations of podosome pairs as a function of distance (19 cells, over 10^4 pairs per cell). *t* test was used to compare pairs under 2 μm and pairs above 2.5 μm. *$p < 0.0001$.

averaged over the entire duration of the tracking (see details in the Methods section). The resulting coefficient $c_{ij}(0)$ is comprised between +1 and −1, which correspond to *i* and *j* being in phase synchrony *versus* out-of-phase synchrony, respectively. Its values calculated for multiple pairs of protrusion force curves and plotted as a function of pair distance are skewed toward positive values for close pairs of podosomes (Figure 5c,d), meaning that close podosomes are more frequently correlated than podosomes farther apart.

As protrusion force is intimately related to core F-actin polymerization,[13−15] we sought to investigate

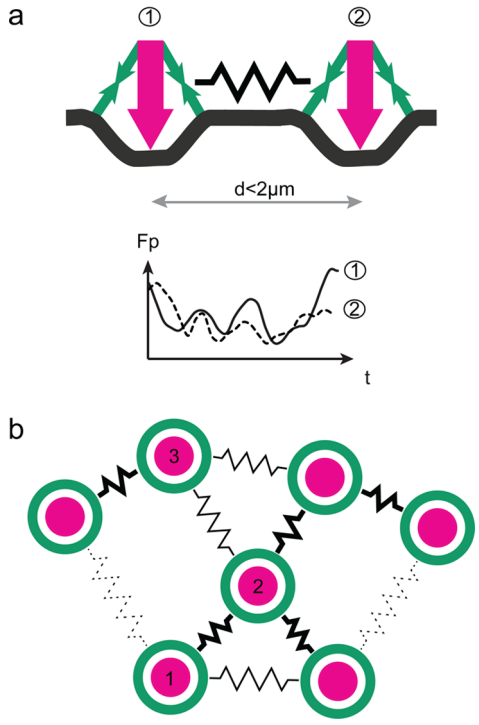

Figure 6. A physical model of podosome spatial synchrony. (a) By simultaneous application of acto-myosin-based traction at the ring (green arrows) and actin polymerization against the substrate at the core (pink arrow), single podosomes generate a dynamic protrusive force that deforms the substrate orthogonally. Physical bonding between podosomes closer than 2 μm causes a mechanical coupling (black spring), leading to the synchrony of podosome direct neighbors. (b) The closer podosomes are, the stronger their interaction and coordination. For instance, direct neighbors (pairs 1−2 or 2−3) are linked (black springs) and tend to present a synchronous behavior, whereas distant podosomes (pair 1−3) show no correlation.

whether actin intensity shows a similar correlated behavior at short distances. mCherry-Lifeact-expressing macrophages were imaged by time-lapse TIRF microscopy (Figure 5e) and podosome dynamics were then tracked to yield individual actin intensity curves over time (Figure 5f). Imaging whole cells instead of small regions made it possible to process a far greater number of pairs of podosomes on which we again performed cross-correlation analysis. When the coefficient $c_{ij}(0)$ is plotted with respect to interpodosome distance, the data display a definite skew at short distances toward positive values of correlation (Figure 5g), corroborating the force dynamics results. Figure 5g indeed shows that core F-actin intensity of close pairs of podosomes (under 2 μm) fluctuates more often in a synchronous manner than that of pairs of podosomes farther apart (above 2.5 μm), the correlation values of which are dispersed and seem symmetrically distributed around zero.

To ascertain that this behavior indicated phase synchrony and not just delayed temporal correlation, the cross-correlation coefficient $c_{ij}(\delta)$ of actin intensity curves of podosomes *i* and *j* was calculated with varying time lag δ. The time lag yielding the maximal value on individual $c_{ij}(\delta)$ curves showed that the cross-correlation was indeed highest for $\delta = 0$ (Figure S1a, Supporting Information). This means that coordination operates within a 2s-long interval and supports the conclusion of phase synchrony. Over 19 cells and 10^5 podosome pairs, the average synchrony coefficient shows a clear decrease with increasing pair distance and stabilizes close to zero as from 2.5 μm (Figure 5h).

Of note, analysis of podosomes in cells expressing mRFP-actin instead of mCherry-Lifeact led to similar behavior (Figure S1b), controlling that Lifeact turnover is not responsible for the intensity correlations but most probably reflects actual actin variation. Given that force measurements were performed on Formvar and not on glass as for fluorescence intensity analysis, we also verified that podosomes of cells plated on the suspended Formvar membrane displayed spatial synchrony (Figure S1c).

Altogether, these results show that force and actin content vary in phase synchrony for podosome pairs under 2 μm. This suggests that synchronization occurs mainly between podosome first neighbors.

CONCLUSION

In the present work, using the protrusion force microscopy method developed previously to measure nanoscale protrusion forces, we have been able to quantify spatial correlations in temporal force dynamics. Our approach consists in combining high-resolution imaging and numerical simulations to automatically convert AFM topographical data into nanoscale force measurements. This method has helped demonstrate the temporal correlation of force production between close pairs of podosomes. We have also provided evidence of spatial synchrony for actin intensity variation of close podosome pairs. Force and actin dynamics may be viewed as instances of the same phenomenon: the podosome core F-actin columnar bundle polymerizes against the Formvar membrane in an oscillatory manner and protrudes onto it. This work emphasizes that podosomes close to each other tend to polymerize, push and protrude in phase synchrony (Figure 6).

Synchrony in a collective system has been studied in very diverse settings,[26−29] among which mechanical and electronic appliances, physiological and cellular rhythms,[30] microarrays and microfluidic reactors,[31,32] and of course theoretical models.[33] The particular feature of the present system is the dependence of synchrony on distance, for its empirical occurrence is scarcer than uniform or pairwise synchrony. Various theoretical explanations of spatial synchrony have been explored.[26,27] For instance out-of-equilibrium collective systems based on the reaction-diffusion model can be tailored to produce collective fluctuating

systems exhibiting dynamic patterns and waves[32] or decrease of coherence with distance throughout a continuous medium.[34] Alternatively, synchronization phenomena accounted for by phase-locking between periodic oscillators may involve pairwise coupling, especially in mechanical systems, or global forcing.[28,31] Finally, short-scale synchrony might also emerge from the spatial distribution of synchronized elements in sparse clusters.[27] However, it is not clear which of these models could explain the synchrony between close podosomes. Chemical microenvironments affecting the actin polymerization rate of podosome subgroups through, for instance, the local concentration of a regulator protein would require a concentration gradient steep enough to maintain different states (*i.e.*, pushing *vs* nonpushing) on the micron scale, yet stable enough to last at least 30 s. Alternatively, phase synchrony between close podosomes supports the hypothesis of a fast coordination, which could proceed from local physical interactions. Physical bonding through the interpodosome actin cables or the plasma membrane could certainly cause a mechanical coupling of *a priori* uncorrelated oscillators, leading to their synchronization, as in the historical example of Huygens' clocks. Whether the spatial synchrony we report here proceeds from direct mechanical interactions between neighbors or local environmental conditions will have to be sustained by further investigation. Dedicated modeling shall also be called for to identify the relevant coupling parameters and formulate an integrated scheme of collective podosome dynamics.

Beyond the progression of our knowledge about podosome mechanics and collective behavior, this work brings new perspective to other research fields in which spatially organized protruding cell structures might operate together to perform a specific function. For example, during the process of transcellular diapedesis, lymphocytes migrate through the endothelium by using clusters of actin-rich protrusions into the endothelial cells.[35] Similar structures have been involved in antigen recognition by T cells probing the endothelium, leading to the formation of a podosynapse.[36] Cell fusion of osteoclast precursors into giant cells and of myoblasts into myotubes involve organized clusters of invasive actin protrusions.[37−39] Endothelial cells are able to form rosettes of podosomes to regulate vascular branching *in vivo*.[40] In frustrated phagocytosis, macrophages enclose opsonised micropatterns within a girdle of podosome-like structures[41] that may be seen as templates for the coordinated actin projections used in actual phagocytosis.[42] The hallmark of such collective structuring is found in osteoclasts. In these cells, podosomes assemble in spatially organized superstructures called sealing zones in order to resorb bone.[20] These superstructures present a meshwork of closely interwoven actin filaments, among which emerge podosome cores connected by denser actin bundles than those connecting disperse podosomes.[18,43] Interestingly, time-lapse observations show that sealing zones display coordinated expansion/contraction cycles.[44] Furthermore, the podosome belt constitutes a tight seal of the area enclosed,[45] which undoubtedly involves powerful adhesion to the substrate; but it may also make use of mechanical pressure by a ring of protrusion-traction devices. In the light of our results, these features might be regulated by the close coordination of individual podosomes working together within the sealing zone.

In conclusion, our study exposes spatiotemporal organization in actin-based protrusive structures in macrophages called podosomes. This paves the way for a better understanding of collective organization in cytoskeletal assemblies, of its functional implications in numerous cell processes and of its mechanisms. Assuredly, podosomes constitute a two-dimensional self-assembled system that calls for the investigation of spatial synchrony from a joint mechanical and biological perspective.

METHODS

Cell Preparation. Human monocytes were isolated from the blood of healthy donors and differentiated into macrophages as previously described.[46] After 7 days of differentiation, human macrophages were trypsinized (Invitrogen) and seeded at 4.5×10^4 cells·cm^{-2} on glass coverslips and on Formvar-coated grids in RPMI medium containing antibiotics.

Time-lapse fluorescence experiments used Lifeact and fluorescent actin as probes. Transduction of mCherry-Lifeact by infection benefited from the constructions designed by Lizarraga and co-workers,[47] which were cloned into a lentiviral vector by the BiVic facility (Toulouse, France). 2−3 days before experiment, monocyte-derived macrophages were incubated in 800 μL of medium in the presence of lentiviral vector (MOI = 1) and 50 μg/mL of protamine sulfate for 1.5 h, after which 1.2 mL of complete medium was added. Cells were detached and then plated in a glass-bottom Lab-TeK observation chamber (Nunc, Roskilde, Denmark) 2 h before observation.

Monocyte-derived macrophages were transfected 4 h before observation with mRFP-actin using a Neon MP5000 electroporation system (Invitrogen) with the following parameters: two 1000 V, 40 ms pulses, with 1 μg of DNA for 2×10^5 cells. They were then plated in a Lab-TeK observation chamber.

Protrusion Force Microscopy (PFM) Measurements. PFM measurements were performed as previously described.[13] Briefly, ethanol-cleaned glass slides were dipped into a Formvar solution of 0.5% (w/v) ethylene dichloride (Electron Microscopy Science). After a few seconds, the Formvar solution was emptied from the film casting device using a calibrated downward flow. After drying of the slides, the film was detached from the slide by contact with water and was left floating at the surface. Acetone-washed 200-mesh nickel grids (EMS) were arranged on floating films, picked up coated with the film onto another glass slide and then air-dried. To evaluate the thickness of the Formvar membrane, the border of Formvar remaining on the glass slide after removing the grids was imaged in contact mode by AFM.

AFM measurements were performed using silicon nitride cantilevers (MLCT-AUHW, Veeco Instruments) with a nominal spring constant of 0.01 $N \cdot m^{-1}$ mounted on a NanoWizard III AFM (JPK Instruments) coupled to an inverted optical microscope (Axiovert 200, Carl Zeiss). To ensure reproducibility in force application, the cantilever sensitivity and spring constant were calibrated before each experiment using the JPK Instrument software using the thermal noise method.[48] For AFM analysis of living cells seeded on Formvar-coated grids, a temperature-controlled was used (Petri dish heater, JPK Instruments) and the culture medium (RPMI 1640 containing 10% FCS and antibiotics) was supplemented with 10 mM HEPES (pH = 7.4) (Sigma-Aldrich). Images were recorded in contact mode in liquid at scanning forces lower than 1 nN with a pixel resolution from 128 to 256 px at line rate from 2 to 20 Hz depending on the scanned area (the size ranged from 3×3 μm to 80×80 μm).

Automated Deformation Height Measurements from AFM Imaging. For height measurements of podosome-induced protrusions, a polynomial correction by line and surface (order 3) of the topographical image was performed to level the image using the JPK Image Processing software. Using an ImageJ macro, the resulting height image was scaled to the actual dimensions, then median-filtered (2 px radius) and scanned for maxima. After manual validation of the detected protrusions, the location of the peak of each protrusion was measured as the gray-level center of mass in a radius of 250 nm around the maximum. To measure the local profile of the deformation, a 4 μm-long, 3 px-wide line was drawn across each peak and rotated in 45° steps, except when the lines were parallel to the direction of movement of the AFM tip. The final deformation profile was taken as the average profile over all of these directions.

For time-lapse measurements, the same steps were carried out for each of the successive PFM images and bulges, the spatial movement of which is small, were then identified from an image to the other.

Finite Element Simulations. Simulations of the Formvar sheet deformation were performed using the Structural Mechanics module of COMSOL Multiphysics 4.3 software (COMSOL France).

Formvar was defined as an elastic material possessing a density of 6.25 $kg \cdot m^{-3}$ and a biaxial Young's modulus of 2.3 GPa as measured previously.[13] A circular Formvar sheet of diameter 15 μm and thickness h_f was clamped at its borders. To model the effect of podosome action on this substrate, an array of two-component modules were defined over one surface of the sheet, composed of a central disc (radius r_p) and a concentric ring (radius r_t and width w) (see Figure 1d,e). To account for neighbor-induced effects, thirty-seven disc-ring modules were arranged in three concentric rings in a hexagonal lattice on one surface of the sheet, with each pair of neighbors separated from each other by a center-to-center distance d. Disc and ring domains were subjected respectively to an upward force F_p and a downward force $F_t = -(1 + \alpha)F_p$ (Figure 1d,e), where the correction factor $\alpha \in [3 \times 10^{-4}; 7 \times 10^{-3}]$ was empirically chosen for each simulation so that the seven central bulges were located in the same plane. A tetrahedral mesh was defined differentially on small (discs and rings) and large (the rest of the sheet) regions, so as to decrease computation time. Provided there were at least two tetrahedrons along the smallest distance in a given region, the size of the mesh elements had no influence on the deformation profile.

ImageJ Macro. The final procedure for the evaluation of protrusion force from AFM topography measurements has been implemented into an ImageJ macro so as to provide automatic processing of AFM data (see source code in Supporting Information). On the basis of the simulations, the force corresponding to a protrusion may be determined using the relation $F = C_0 \cdot E/(1 - \nu^2) \cdot h_f^3/r_t^2 \cdot h$. The experimental values of membrane thickness h_f and ring radius r_t are to be entered as input parameters, and the value of C_0 has been integrated in the code where it can be modified when necessary. The deformation profile of each protrusion is then measured on the AFM image automatically as described above, in order to compute the deformation height h defined as the difference between peak height and height at ring radius (Figure 1f). Finally, h is converted to force by the above formula.

Immunofluorescence Imaging of Fixed Cells. After macrophages had been plated for 3 h on glass coverslips, the medium was replaced by a hypotonic buffer of distilled water and 10 μg/mL phalloidin (Sigma-Aldrich) at 37 °C for 30s, and then the cells were flushed 10 times before being fixed with a 4% paraformaldehyde solution in phosphate buffer saline 1× (Fisher Scientific). F-actin was visualized *via* AlexaFluo Texas red-phalloidin (Invitrogen, 1/500), and vinculin was revealed with a monoclonal antivinculin antibody (M3191, Sigma, 1/500) and visualized with an AlexaFluo 488-coupled secondary antibody. Using a 100× objective lens (NA = 1.45) mounted on a Nikon Eclipse Ti-E, and an Andor sCMOS Neo camera in high dynamic mode and in global shutter, a series of nine images at 100 nm interval was acquired on each field. These images were processed by nonlinear deconvolution to reduce optical distortion, using the Richardson−Lucy algorithm with total variation regularization[49] implemented as a plugin in the ImageJ software *Deconvolution Lab*.[50] The total variation regularization parameter, a constraint which suppresses unstable oscillations while preserving object edges, was determined from each image using the method described by Laasmaa and coworkers.[51] To estimate the end of the iterations, the difference threshold between two successive iterations was defined as 10^{-6}. Furthermore, a positivity constraint was applied based on the realistic hypothesis that the fluorescent signal is only positive. Zero padding served to increase the support of the optical transfer function before the deconvolution process. An adaptive estimation of the zero-frequency components of the noise was estimated for each image in the regions without cells. Thirty experimental point spread functions were averaged and used for inversion after removal of the zero-frequency components of the noise.

Automated Measurements of Podosome Geometry from Fluorescence Imaging. Pairs of deconvolved fluorescence images of actin cores and vinculin rings (Figure 3a−d) served to automatically measure the geometrical parameters of podosomes (core and ring radii and ring width) using a dedicated ImageJ macro. The position of the center of each core was located by scanning the actin image for intensity maxima (FindMaxima plugin) and weighting the result with the surrounding gray values. Its radius r_c was then defined on its radial intensity profile as the distance from the center to the inflection point, which could be determined on the actin edge image, *i.e.*, the map of highest intensity variation produced by the FindEdges plugin (Figure 3e,g). As most actin cores were not perfectly circular, the final value for the core radius was chosen as the median value of the radii measured in eight directions from the center (each 45° angle). Similarly, the radial intensity profiles of vinculin rings revealed the ring characteristics: on the one hand, the ring radius r_r was measured as the distance from the center of the core to the vinculin intensity peak (Figure 3j), and on the other hand, the ring width w was given by the distance between the twin inflection points closest to the peak, *i.e.*, the two peaks of each radial profile of the edge image: $w = r_e - r_i$ (Figure 3j).

To determine interpodosome distance, the Delaunay triangulation of podosomes was obtained from actin fluorescence images segmented for core centers (Figure 3q). Each Delaunay triangle is defined as a triangle of three cores whose circumcircle encloses no other core,[25] a simple iterative algorithm based on this definition served to calculate the triangulation (Figure 3r). This made it possible to define, for each podosome, its neighbors as the podosomes connected by a Delaunay edge, without imposing any distance threshold. The interpodosome distance was then chosen as the average distance to these neighbors.

Scanning Electron Microscopy of Inverted Macrophages. For scanning electron microscopy observations of podosomes, macrophages plated on polydimethylsiloxane (PDMS) (Sylgard 184, Dow Corning) substrates were fixed with glutaraldehyde and inverted as per the protocol described by Gudzenko and Franz.[52] More precisely, the sample was first dehydrated through a graded series of ethanol (35−100%) and dried with gentle nitrogen flow. A small drop of optical adhesive (OP-29,

Dymax) was applied onto the sample and covered with a glass coverslip. After the adhesive was exposed to UV light (365 nm) for 5 min, the PDMS slab was delicately peeled off, while the cells remained upside-down on the now solid adhesive. Preparations were then washed three times for 5 min in 0.2 M cacodylate buffer (pH 7.4), postfixed for 1 h in 1% (wt/vol) osmium tetroxide in 0.2 M cacodylate buffer (pH 7.4), and washed with distilled water. Samples were dehydrated through a graded series (25−100%) of ethanol, transferred in acetone and subjected to critical point drying with CO_2 in a Leica EM CPD300. Dried specimens were sputter-coated with 3 nm platinum with a Leica EM MED020 evaporator and were examined and photographed with a FEI Quanta FEG250.

The area A_{SEM} of the protruding regions (Figure 3n,o) was measured manually using ImageJ and then converted into a podosome radius by $r_{SEM} = (A_{SEM}/\pi)^{1/2}$.

Time-Lapse Fluorescence Imaging of Live Cells. Podosome dynamics inside live macrophages were visualized using a TIRF microscopy setup (Olympus FV1000). 2 h before observation, cells were detached using trypsin-EDTA and plated inside thin cover-glass-bottomed Lab-Tek chambers (Fisher Scientific) in complete medium. Imaging was carried out using an inverted IX-81 microscope with a 60× immersion objective (NA = 1.49) and an Orca-R2 camera (Hamamatsu). A "Box-Cube-Brick" set (Life Imaging Systems) served to stabilize temperature (37 °C) and CO_2 pressure (5%). For time-lapse observation on Formvar, cells were prepared as for PFM measurements and imaged on a DMIRB fluorescence microscope (Leica) using a 63× immersion objective (NA = 1.3) and a CoolSNAP HQ2 (Roper Scientific). Except when otherwise specified, each cell was filmed during 10 min with images every 2s.

Preliminary processing of image sequences with the Fiji software includes registration using the StackReg plugin[53] and subtraction of background intensity (default ImageJ function). Podosome tracking and further analyses were then performed with ImageJ. Briefly, each podosome i was located and tracked over its lifetime and its spatial coordinates and raw fluorescence intensity were measured for each time point t. After subtraction of cellular background (measured at each time point), raw intensity was fitted with a decreasing exponential function which was further subtracted to eliminate photobleaching. Final grayscale actin intensity values were taken as the average intensity over two successive time points.

Quantification of Synchronous Variation by Cross-Correlation Analysis. To estimate the spatial correlation of signal temporal variation between pairs of podosomes, Pearson cross-correlation coefficients were calculated over a 1 min-long window sliding along the image sequence. A synchrony estimator of the podosome pair was then defined as the average value of this series of Pearson coefficients.

More specifically, denoting by $u_i(t)$ the value of either force or actin intensity of podosome i at time t (the signal), T the length of the image sequence, 2τ that of the sliding window and δ the time lag, the estimator $c_{ij}(\delta)$ between functions u_i and u_j was defined as

$$c_{ij}(\delta) = \frac{1}{T - 2\tau - 2|\delta|} \sum_{t=\tau+1+|\delta|}^{T-\tau-|\delta|} C_t^{(\delta)}(u_i, u_j)$$

where $C_t^{(\delta)}(u_i, u_j)$ denotes the Pearson cross-correlation coefficient between u_i and δ-delayed u_j over the window $[t - \tau, t + \tau]$, *i.e.*,

$$C_t^{(\delta)}(u_i, u_j) = \frac{\sum_{k=t-\tau}^{t+\tau} (u_i(k) - \overline{u}_i)\cdot(u_j(k+\delta) - \overline{u}_j)}{\sqrt{\sum_{k=t-\tau}^{t+\tau} (u_i(k) - \overline{u}_i)^2 \cdot \sum_{k=t-\tau}^{t+\tau} (u_j(k+\delta) - \overline{u}_j)^2}}$$

which is exactly the covariance of function u_i restricted to $[t - \tau, t + \tau]$ with function u_j restricted to $[t - \tau + \delta, t + \tau + \delta]$, normalized by their standard deviations over these respective intervals. This definition implies $-1 \leq c_{ij}(\delta) \leq 1$, with $+1$ indicating perfect correlation (phase synchrony), -1 perfect anticorrelation (out-of-phase synchrony) and 0 statistical orthogonality. The undelayed correlation indicator $c_{ij}(0)$ indicates correlation with no time lag and was thus referred to as the synchrony coefficient between u_i and u_j.

To avoid irrelevant high correlation values, pairs of podosomes were only analyzed when they shared a common existence of at least 2 min and when the relative amplitude of signal variation $(\max u - \min u)/\overline{u}$ was above 10% for each podosome.

Conflict of Interest: The authors declare no competing financial interest.

Acknowledgment. The authors are grateful to S. Balor for Formvar membrane preparation; to S. Tournier for allowing the use of her Nikon Eclipse; to D. Zerbib for his UV generator; and to S. Gerchinovitz and S. Déjean for their helpful advice on statistical analysis. A.P. would like to thank A. Bhaswara for his kind explanations regarding meshing in COMSOL. The authors also acknowledge the TRI imaging facility. This work has been supported in part by la Fondation pour la Recherche Médicale (FRM DEQ-2011-0421312), l'Agence Nationale de la Recherche (ANR 2010-01301 and ANR14-CE11-0020-02) and the European Community's Seventh framework program under Grant Agreement HEALTH-F4-2011-282095-Tarkinaid.

Supporting Information Available: Figure S1 and the source code of the ImageJ macro of protrusion force evaluation from AFM topographical data. Figure S1: (a) Left: cross-correlation coefficient of some actin intensity curves of podosomes i and j as a function of time lag δ for individual (i,j) pairs. Right: histogram of the values of $|\delta|$ that maximize $c_{ij}(\delta)$, over all pairs of curves corresponding to Figure 5g such that $c_{ij}(0) \geq 0.3$. (b) Cells expressing mRFP-actin and observed by TIRF microscopy display the same behavior as those stained with mCherry-Lifeact (Figure 5h). Plotted is the average synchrony coefficient (±s.d.) of fluorescence intensity fluctuations of podosome pairs as a function of distance (6 cells, over 10^4 pairs per cell). t test was used to compare pairs under 2 μm and pairs above 2.5 μm. $^*p < 0.0001$. (c) Cells expressing mCherry-Lifeact plated on a suspended Formvar membrane and observed by epifluorescence microscopy display the same behavior as those plated on glass and observed by TIRF microscopy (Figure 5h). Plotted is the average synchrony coefficient (±s.d.) of fluorescence intensity fluctuations of podosome pairs as a function of distance (5 cells, over 10^4 pairs per cell). t test was used to compare pairs under 2 μm and pairs above 2.5 μm. $^*p < 0.0001$. This material is available free of charge *via* the Internet at http://pubs.acs.org.

REFERENCES AND NOTES

1. Harris, A. K.; Wild, P.; Stopak, D. Silicone Rubber Substrata: A New Wrinkle in the Study of Cell Locomotion. *Science* **1980**, *208*, 177–179.
2. Balaban, N. Q.; Schwarz, U. S.; Riveline, D.; Goichberg, P.; Tzur, G.; Sabanay, I.; Mahalu, D.; Safran, S.; Bershadsky, A.; Addadi, L.; *et al.* Force and Focal Adhesion Assembly: A Close Relationship Studied Using Elastic Micropatterned Substrates. *Nat. Cell Biol.* **2001**, *3*, 466–472.
3. Butler, J. P.; Tolić-Nørrelykke, I. M.; Fabry, B.; Fredberg, J. J. Traction Fields, Moments, and Strain Energy That Cells Exert on Their Surroundings. *Am. J. Physiol.: Cell Physiol.* **2002**, *282*, C595–605.
4. Tan, J. L.; Tien, J.; Pirone, D. M.; Gray, D. S.; Bhadriraju, K.; Chen, C. S. Cells Lying on a Bed of Microneedles: An Approach to Isolate Mechanical Force. *Proc. Natl. Acad. Sci. U. S. A.* **2003**, *100*, 1484–1489.
5. Geiger, B.; Bershadsky, A. Assembly and Mechanosensory Function of Focal Contacts. *Curr. Opin. Cell Biol.* **2001**, *13*, 584–592.
6. Kraning-Rush, C. M.; Carey, S. P.; Califano, J. P.; Reinhart-King, C. A. Quantifying Traction Stresses in Adherent Cells. *Methods Cell Biol.* **2012**, *110*, 139–178.
7. Linder, S. Invadosomes at a Glance. *J. Cell Sci.* **2009**, *122*, 3009–3013.
8. Linder, S.; Wiesner, C. Tools of the Trade: Podosomes as Multipurpose Organelles of Monocytic Cells. *Cell. Mol. Life Sci.* **2014**, *72*, 121–135.

9. Destaing, O.; Saltel, F.; Géminard, J. C.; Jurdic, P.; Bard, F. Podosomes Display Actin Turnover and Dynamic Self-Organization in Osteoclasts Expressing Actin-Green Fluorescent Protein. *Mol. Biol. Cell* **2003**, *14*, 407–416.
10. Kopp, P.; Lammers, R.; Aepfelbacher, M.; Woehlke, G.; Rudel, T.; Machuy, N.; Steffen, W.; Linder, S. The Kinesin Kif1c and Microtubule Plus Ends Regulate Podosome Dynamics in Macrophages. *Mol. Biol. Cell* **2006**, *17*, 2811–2823.
11. Badowski, C.; Pawlak, G.; Grichine, A.; Chabadel, A.; Oddou, C.; Jurdic, P.; Pfaff, M.; Albigès-Rizo, C.; Block, M. R. Paxillin Phosphorylation Controls Invadopodia/Podosomes Spatiotemporal Organization. *Mol. Biol. Cell* **2008**, *19*, 633–645.
12. Collin, O.; Na, S.; Chowdhury, F.; Hong, M.; Shin, M. E.; Wang, F.; Wang, N. Self-Organized Podosomes Are Dynamic Mechanosensors. *Curr. Biol.* **2008**, *18*, 1288–1294.
13. Labernadie, A.; Bouissou, A.; Delobelle, P.; Balor, S.; Voituriez, R.; Proag, A.; Fourquaux, I.; Thibault, C.; Vieu, C.; Poincloux, R.; *et al.* Protrusion Force Microscopy Reveals Oscillatory Force Generation and Mechanosensing Activity of Human Macrophage Podosomes. *Nat. Commun.* **2014**, *5*, 5343.
14. Gawden-Bone, C.; Zhou, Z.; King, E.; Prescott, A.; Watts, C.; Lucocq, J. Dendritic Cell Podosomes Are Protrusive and Invade the Extracellular Matrix Using Metalloproteinase Mmp-14. *J. Cell Sci.* **2010**, *123*, 1427–1437.
15. Luxenburg, C.; Winograd-Katz, S.; Addadi, L.; Geiger, B. Involvement of Actin Polymerization in Podosome Dynamics. *J. Cell Sci.* **2012**, *125*, 1666–1672.
16. van den Dries, K.; Meddens, M. B.; de Keijzer, S.; Shekhar, S.; Subramaniam, V.; Figdor, C. G.; Cambi, A. Interplay between Myosin Iia-Mediated Contractility and Actin Network Integrity Orchestrates Podosome Composition and Oscillations. *Nat. Commun.* **2013**, *4*, 1412.
17. Yu, C. H.; Rafiq, N. B.; Krishnasamy, A.; Hartman, K. L.; Jones, G. E.; Bershadsky, A. D.; Sheetz, M. P. Integrin-Matrix Clusters Form Podosome-Like Adhesions in the Absence of Traction Forces. *Cell Rep.* **2013**, *5*, 1456–1468.
18. Luxenburg, C.; Geblinger, D.; Klein, E.; Anderson, K.; Hanein, D.; Geiger, B.; Addadi, L. The Architecture of the Adhesive Apparatus of Cultured Osteoclasts: From Podosome Formation to Sealing Zone Assembly. *PloS One* **2007**, *2*, e179.
19. van den Dries, K.; Schwartz, S. L.; Byars, J.; Meddens, M. B.; Bolomini-Vittori, M.; Lidke, D. S.; Figdor, C. G.; Lidke, K. A.; Cambi, A. Dual-Color Superresolution Microscopy Reveals Nanoscale Organization of Mechanosensory Podosomes. *Mol. Biol. Cell* **2013**, *24*, 2112–2123.
20. Jurdic, P.; Saltel, F.; Chabadel, A.; Destaing, O. Podosome and Sealing Zone: Specificity of the Osteoclast Model. *Eur. J. Cell Biol.* **2006**, *85*, 195–202.
21. Schachtner, H.; Calaminus, S. D.; Thomas, S. G.; Machesky, L. M. Podosomes in Adhesion, Migration, Mechanosensing and Matrix Remodeling. *Cytoskeleton* **2013**, *70*, 572–589.
22. Cox, S.; Rosten, E.; Monypenny, J.; Jovanovic-Talisman, T.; Burnette, D. T.; Lippincott-Schwartz, J.; Jones, G. E.; Heintzmann, R. Bayesian Localization Microscopy Reveals Nanoscale Podosome Dynamics. *Nat. Methods* **2012**, *9*, 195–200.
23. Walde, M.; Monypenny, J.; Heintzmann, R.; Jones, G. E.; Cox, S. Vinculin Binding Angle in Podosomes Revealed by High Resolution Microscopy. *PloS One* **2014**, *9*, e88251.
24. Timoshenko, S.; Woinowsky-Krieger, S. *Theory of Plates and Shells*, 2nd ed.;McGraw-Hill: New York, 1959; p 4−6.
25. Delaunay, B. Sur La Sphère Vide. *Bull. Acad. Sci. URSS* **1934**, 793–800.
26. Liebhold, A.; Koenig, W. D.; Bjørnstad, O. N. Spatial Synchrony in Population Dynamics. *Annu. Rev. Ecol. Evol. Syst.* **2004**, *35*, 467–490.
27. Rosenblum, M.; Pikovsky, A. Synchronization: From Pendulum Clocks to Chaotic Lasers and Chemical Oscillators. *Contemp. Phys.* **2003**, *44*, 401–416.
28. Strogatz, S. H. Exploring Complex Networks. *Nature* **2001**, *410*, 268–276.
29. Vanag, V. K.; Yang, L.; Dolnik, M.; Zhabotinsky, A. M.; Epstein, I. R. Oscillatory Cluster Patterns in a Homogeneous Chemical System with Global Feedback. *Nature* **2000**, *406*, 389–391.
30. Goldbeter, A.; Gerard, C.; Gonze, D.; Leloup, J. C.; Dupont, G. Systems Biology of Cellular Rhythms. *FEBS Lett.* **2012**, *586*, 2955–2965.
31. Taylor, A. F.; Tinsley, M. R.; Wang, F.; Huang, Z.; Showalter, K. Dynamical Quorum Sensing and Synchronization in Large Populations of Chemical Oscillators. *Science* **2009**, *323*, 614–617.
32. Thutupalli, S.; Herminghaus, S. Tuning Active Emulsion Dynamics *via* Surfactants and Topology. *Eur. Phys. J. E: Soft Matter Biol. Phys.* **2013**, *36*, 91.
33. Winfree, A. T. Biological Rhythms and the Behavior of Populations of Coupled Oscillators. *J. Theor. Biol.* **1967**, *16*, 15–42.
34. Wang, H.; Ouyang, Q. Spatiotemporal Chaos of Self-Replicating Spots in Reaction-Diffusion Systems. *Phys. Rev. Lett.* **2007**, *99*, 214102.
35. Carman, C. V.; Sage, P. T.; Sciuto, T. E.; de la Fuente, M. A.; Geha, R. S.; Ochs, H. D.; Dvorak, H. F.; Dvorak, A. M.; Springer, T. A. Transcellular Diapedesis Is Initiated by Invasive Podosomes. *Immunity* **2007**, *26*, 784–797.
36. Sage, P. T.; Varghese, L. M.; Martinelli, R.; Sciuto, T. E.; Kamei, M.; Dvorak, A. M.; Springer, T. A.; Sharpe, A. H.; Carman, C. V. Antigen Recognition Is Facilitated by Invadosome-Like Protrusions Formed by Memory/Effector T Cells. *J. Immunol.* **2012**, *188*, 3686–3699.
37. Sens, K. L.; Zhang, S.; Jin, P.; Duan, R.; Zhang, G.; Luo, F.; Parachini, L.; Chen, E. H. An Invasive Podosome-Like Structure Promotes Fusion Pore Formation During Myoblast Fusion. *J. Cell Biol.* **2010**, *191*, 1013–1027.
38. Takito, J.; Nakamura, M.; Yoda, M.; Tohmonda, T.; Uchikawa, S.; Horiuchi, K.; Toyama, Y.; Chiba, K. The Transient Appearance of Zipper-Like Actin Superstructures During the Fusion of Osteoclasts. *J. Cell Sci.* **2012**, *125*, 662–672.
39. Shilagardi, K.; Li, S.; Luo, F.; Marikar, F.; Duan, R.; Jin, P.; Kim, J. H.; Murnen, K.; Chen, E. H. Actin-Propelled Invasive Membrane Protrusions Promote Fusogenic Protein Engagement During Cell-Cell Fusion. *Science* **2013**, *340*, 359–363.
40. Seano, G.; Chiaverina, G.; Gagliardi, P. A.; di Blasio, L.; Puliafito, A.; Bouvard, C.; Sessa, R.; Tarone, G.; Sorokin, L.; Helley, D.; *et al.* Endothelial Podosome Rosettes Regulate Vascular Branching in Tumour Angiogenesis. *Nat. Cell Biol.* **2014**, *16*, 931–938.
41. Labrousse, A. M.; Meunier, E.; Record, J.; Labernadie, A.; Beduer, A.; Vieu, C.; Ben Safta, T.; Maridonneau-Parini, I. Frustrated Phagocytosis on Micro-Patterned Immune Complexes to Characterize Lysosome Movements in Live Macrophages. *Front. Immunol.* **2011**, *2*, 1–10.
42. Freeman, S. A.; Grinstein, S. Phagocytosis: Receptors, Signal Integration, and the Cytoskeleton. *Immunol. Rev.* **2014**, *262*, 193–215.
43. Akisaka, T.; Yoshida, H.; Suzuki, R.; Takama, K. Adhesion Structures and Their Cytoskeleton-Membrane Interactions at Podosomes of Osteoclasts in Culture. *Cell Tissue Res.* **2008**, *331*, 625–641.
44. Saltel, F.; Destaing, O.; Bard, F.; Eichert, D.; Jurdic, P. Apatite-Mediated Actin Dynamics in Resorbing Osteoclasts. *Mol. Biol. Cell* **2004**, *15*, 5231–5241.
45. Väänänen, H. K.; Zhao, H.; Mulari, M.; Halleen, J. M. The Cell Biology of Osteoclast Function. *J. Cell Sci.* **2000**, *113*, 377–381.
46. Van Goethem, E.; Poincloux, R.; Gauffre, F.; Maridonneau-Parini, I.; Le Cabec, V. Matrix Architecture Dictates Three-Dimensional Migration Modes of Human Macrophages: Differential Involvement of Proteases and Podosome-Like Structures. *J. Immunol.* **2010**, *184*, 1049–1061.
47. Lizarraga, F.; Poincloux, R.; Romao, M.; Montagnac, G.; Le Dez, G.; Bonne, I.; Rigaill, G.; Raposo, G.; Chavrier, P. Diaphanous-Related Formins Are Required for Invadopodia Formation and Invasion of Breast Tumor Cells. *Cancer Res.* **2009**, *69*, 2792–2800.
48. Hutter, J. L.; Bechhoefer, J. Calibration of Atomic-Force Microscope Tips. *Rev. Sci. Instrum.* **1993**, *64*, 1868–1873.

49. Dey, N.; Blanc-Feraud, L.; Zimmer, C.; Roux, P.; Kam, Z.; Olivo-Marin, J. C.; Zerubia, J. Richardson-Lucy Algorithm with Total Variation Regularization for 3d Confocal Microscope Deconvolution. *Microsc. Res. Technol.* **2006**, *69*, 260–266.
50. Vonesch, C.; Unser, M. A Fast Thresholded Landweber Algorithm for Wavelet-Regularized Multidimensional Deconvolution. *IEEE Trans. Image Process.* **2008**, *17*, 539–549.
51. Laasmaa, M.; Vendelin, M.; Peterson, P. Application of Regularized Richardson-Lucy Algorithm for Deconvolution of Confocal Microscopy Images. *J. Microsc.* **2011**, *243*, 124–140.
52. Gudzenko, T.; Franz, C. M. Inverting Adherent Cells for Visualizing ECM Interactions at the Basal Cell Side. *Ultramicroscopy* **2013**, *128*, 1–9.
53. Thévenaz, P.; Ruttimann, U. E.; Unser, M. A Pyramid Approach to Subpixel Registration Based on Intensity. *IEEE Trans. Image Process.* **1998**, *7*, 27–41.